



Photocatalytic and biocidal activities of novel coating systems of mesoporous and dense TiO₂-anatase containing silver nanoparticles



María V. Roldán^a, Paula de Oña^b, Yolanda Castro^c, Alicia Durán^c, Pablo Faccendini^d, Claudia Lagier^d, Roberto Grau^{b,*}, Nora S. Pellegrini^{a,**}

^a Laboratorio de Materiales Cerámicos, FCEIA-UNR, IFIR-CONICET, Pellegrini 250, Rosario S2000BTP, Argentina

^b Laboratorio de Microbiología Molecular, FCByF-UNR-CONICET, Suipacha 531, Rosario S2002LRK, Argentina

^c Instituto de Cerámica y Vidrio (CSIC), Campus de Cantoblanco, 28049, Madrid, Spain

^d IQUIR-UNR-CONICET, Suipacha 531, Rosario S2002LRK, Argentina

ARTICLE INFO

Article history:

Received 16 April 2014

Received in revised form 13 June 2014

Accepted 15 July 2014

Available online 23 July 2014

Keywords:

Silver nanoparticles

Sol-gel film

Titania

Photocatalysis

Bactericidal

Sporocidal

ABSTRACT

Here we describe the development of novel nanostructured coating systems with improved photocatalytic and antibacterial activities. These systems comprise a layer of SiO₂ followed by a layer of mesoporous or dense TiO₂-anatase, and doping with silver nanoparticles (Ag NPs). The coatings were synthesized via a sol-gel technique by combining colloidal Ag NPs with TiO₂ and SiO₂ sols.

The photocatalytic activity was studied through methyl orange decomposition under UV light. Results showed a great increase of photocatalytic activity by Ag NPs doping. The most active photocatalyst corresponded to the Ag-SiO₂/TiO₂ mesoporous system, associated with the porosity of the coatings and with the decrease of e-h recombination for the presence of Ag NPs.

All the TiO₂ coatings showed a strong bactericidal activity against planktonic forms of Gram-negative (enterohemorrhagic *Escherichia coli*) and Gram-positive (*Listeria monocytogenes*) pathogens, as well as a strong germicidal effect against deadly spores of human gas gangrene- and anthrax-producing bacteria (*Clostridium perfringens* and *Bacillus anthracis*, respectively). The bactericidal and sporocidal activity was improved by doping the coatings with Ag NPs, even more when nanoparticles were in the outer layer of TiO₂, because they are more accessible to the environment.

The mechanisms responsible for the increase of photocatalytic and bactericidal behaviors related to Ag NP doping were studied by spectroscopic ellipsometry, UV-vis spectroscopy, photoluminescence and anodic stripping voltammetry. It was found that the separation of the electron-hole pair contributed to the enhancement of photocatalysis, whereas the effect of the local electric field reinforcement was probably present. A possible involvement of a decrease of band-gap energy and dispersion by silver nanoparticles is ruled out. Bactericidal efficacy was increased by Ag⁺ ion release.

Overall, the results included in this article show that the architecture of the films may tune photocatalytic and bactericidal properties.

© 2014 Elsevier B.V. All rights reserved.

1. Introduction

Continuous changes in everyday life give rise to the exposure of people to higher pollution rates and exposure to a high concentration of harmful bacteria. Therefore, the development of novel photocatalytic materials with a strong and broad microbicidal activity to be applied on water [1,2], surface [3], and air [4] sanitation is appealing. In this respect, nanotechnology [5] has been recently considered an adequate technology to produce nanomaterials with a high specific surface area and reactivity;

thus, nanomaterials are excellent adsorbents, catalysts and/or sensors, and interesting for antimicrobial applications. The morphology of nanomaterials strongly affects the response of microorganisms [6,7], and these characteristics depend on the processing parameters [8–10]. Titanium dioxide (TiO₂) coatings are one of the most interesting materials as photocatalysts due to their properties, such as an excellent optical transparency in the visible and near infrared regions, a high corrosion resistance, chemical and thermal stability and low cost. More recently, the combination of silver with TiO₂ to form films has proved to act as an excellent antimicrobial coating [11]. Silver nanoparticles (Ag NPs) have been used for bactericidal and fungicide applications, as they affect cellular metabolism and inhibit cell growth [12]. Currently, many textiles [13], keyboards, wound dressings, and biomedical devices [14] contain Ag NPs that continuously release a low level of silver ions to provide

* Corresponding author. Tel.: +54 341 4353377.

** Corresponding author. Tel./fax: +54 341 485 3200.

E-mail addresses: robertograu@fulbrightmail.org (R. Grau), pellegrini@fceia.unr.edu.ar (N.S. Pellegrini).

protection against bacteria [15], and new materials are also being developed [16,17].

In particular, sol–gel process is a good alternative to obtain composite nanomaterials. The sol–gel process allows controlling of the synthesis parameters and deposition, as well as the uniform distribution of metal (Ag NPs) that affects the final properties.

In recent years, the resistance of bacteria to antibiotics has increased due to an abundant use of antibiotics in animal feed as growth promoters, as well as their abusive utilization in medicine and veterinary [14]. As a consequence of the emergency in antibiotic-resistance, there is a failure in antibiotic-treatment that results in a significant increase of mortality, morbidity, cost of medical treatments and spreading of infectious bacteria among the human population [14, 18,19]. Bacteria such as *Listeria monocytogenes* and *Escherichia coli* are human-pathogens that account for different diseases that compromise not only the people's lives but also human activities and capabilities after healing. *L. monocytogenes* is one of the most virulent food-borne pathogens, able to survive and multiple at low temperatures [20]. *L. monocytogenes*, typically found in prepared and processed food, causes septicemia, encephalitis, intrauterine or cervical infections in women [21,22]. *L. monocytogenes* is able to survive and multiply within host cells and to spread intracellular infections from one tissue to another, compromising the efficacy of the antibiotic therapy that takes place from outside the infected cells [23]. Pathogenic *E. coli*, in particular enterohemorrhagic isolates – EHEC O157:H7 and O104:H4 – causes bleeding colitis in humans that can progress to hemolytic uremic syndrome (HUS), an important cause of acute renal failure in children and of mortality in adults [24,25]. Humans acquire EHEC through direct contact with animals, their feces or contaminated water, but more commonly via the ingestion of underdone ground beef or contaminated vegetables and fruits [26–28]. The low infectious dose of EHEC needed to produce disease in humans demands appropriate actions to prevent the ingestion of this deadly pathogen by humans [24,26].

The antimicrobial effects of Ag NPs and photocatalytic semiconductor materials against microorganisms in vegetative (planktonic) state as well as in biofilms have been previously reported [7,12, 29–33]. However, there are few reports about the effect of Ag NPs alone or in combination with photocatalytic metal oxides on the most resistant structure that a bacterium is able to develop: the spore cell [34]. Spores are extremely resistant to a variety of harsh treatments; they remain dormant, although viable and ready to germinate, in diverse environments for very long periods of time; and they function as vectors of food spoiling, due to sporulation-related enterotoxin production, and of food-borne disease, as well as of diseases such as anthrax, tetanus and gas gangrene. The susceptibility of the spores of the non-pathogenic bacterium *Bacillus subtilis* [35,36] has been assayed against silver and copper nanoparticles [37, 38] and composites of TiO₂ co-doped with Ag–carbon–sulfur particles [39]. Regarding the susceptibility of spores from pathogenic bacteria, there are reports of the effects of silver nanoparticles against *Clostridium botulinum* [40] spores, and of photocatalytic TiO₂ against *Bacillus cereus*, *Bacillus anthracis* and *Clostridium difficile* spores [41–43]. However, there is only one report, to our best knowledge, that describes the effect of Ag NPs and TiO₂ (Ag–TiO₂ composite) on spores of a pathogenic bacterium (*B. cereus*) [44]. Unfortunately, there are no other studies of the biocidal effects of similar Ag–TiO₂ composites on the survival of other dangerous and persistent spores, such as *B. anthracis* and *Clostridium perfringens* spores, the etiological agents of anthrax and gas gangrene, respectively [45–51]. *C. perfringens* is the third more common cause of food-poisoning in developed countries and it produces diverse infections, ranging from antibiotic-associated diarrhea to tissue necrosis and, eventually, the deadly human gas gangrene [45,46,50,51]. *B. anthracis* is the etiologic agent of anthrax and is also able to form spores [48]. Even though anthrax is a common disease in livestock (cutaneous anthrax) and it rarely causes disease in humans, the

bioterrorist events with inhaled *B. anthracis* spores (causative of respiratory or inhalational anthrax) that happened immediately after the 11S terrorist attack make anthrax a low-cost and deadly bioweapon of highly human concern [47–49]. The contamination of surfaces, even accidental or intentional, with any of these or other pathogens represents an initial route for human infection. An antimicrobial coating able to inactivate not only the vegetative forms but also bacterial spores will contribute to stop the dissemination of bacterial pathogens and prevent the development of diseases.

This paper presents a novel synthesis technique of thin films that results in highly versatile and effective coating structures. The different architectures thus produced introduce silver nanoparticles either into the outer TiO₂ layer (dense or mesoporous) or in the inner layer of SiO₂, providing highly effective photocatalytic and bactericidal behaviors. The sol–gel technique permits to achieve a maximum homogeneity along the coating profile and the nanoparticles are homogeneously distributed all over the layer, not limited to the surface where they are susceptible of oxidation or re-dissolution [52].

Here, we report the development of silver nanoparticles (Ag NPs) doping dense and mesoporous TiO₂, as well as SiO₂ coatings produced by sol–gel. Mesoporous TiO₂ was obtained by the evaporation-induced self-assembly (EISA) method. Ag NPs were first obtained by a colloidal process, and then mixed with sol–gel sols with effective control of particle size distribution and morphology. The photocatalytic activity of different coating structures combining Ag NP doped layers was measured by the degradation of methyl orange under UV light, showing an extremely high efficacy. The bactericidal efficacy of the coatings was assessed against Gram-negative and Gram-positive microorganisms. The mechanisms involved in the enhancement of photocatalytic and bactericidal properties of TiO₂ by silver nanoparticles were investigated with UV–vis spectroscopy, photoluminescence and electrochemical measurements. Under UV-activation, the Ag-doped SiO₂/TiO₂ coatings are significantly more active than non-doped SiO₂/TiO₂ coatings or Ag NPs alone to kill anthrax- and gas gangrene-producing bacterial spores.

2. Experimental

2.1. Preparation of sols and coatings

Silver nanoparticle (Ag NP) colloids were synthesized ex-situ by the reduction of Ag⁺ from AgNO₃ using N-(3-trimethoxysilylpropyl) diethylenetriamine (ATS, Sigma-Aldrich Chemical Co.) or polyvinylpyrrolidone (PVP, Sigma-Aldrich Chemical Co.) as stabilizer and ethanol (Merck) as solvent. More details about the colloidal synthesis have been reported elsewhere [53–55]. Silver colloidal nanoparticles (hereinafter AgATS and AgPVP, depending on the stabilizer used) were stored in a dark environment at room temperature. The colloidal silver suspensions were characterized by Transmission Electronic Microscopy (TEM) with Hitachi H-7100 equipment. Samples for imaging were obtained by depositing a sol drop onto carbon-coated copper grids and evaporating the solvent.

SiO₂ and TiO₂ sols were obtained by a sol–gel process described in [56]. Colloidal AgATS nanoparticles were added to SiO₂ sol to obtain Ag-doped SiO₂ precursor sol with a final concentration of 0.40 M SiO₂ and 0.04 M AgATS. On the other hand, AgPVP nanoparticles were added to the TiO₂ sol in order to obtain the Ag-doped TiO₂ sol, with a final concentration of 0.37 M TiO₂ and 0.037 M AgPVP. TiO₂ mesoporous sol was prepared following the same procedure, but incorporating (polyethyleneglycol)₂₀ hexadecyl ether (Brij58, Sigma-Aldrich Chemical Co.) into the precursor TiO₂ sol [56].

Multilayer coatings were obtained by dip-coating onto a soda-lime glass substrate (microscope slide) by depositing a SiO₂ layer followed by a TiO₂ layer, both with and without Ag NPs. (Fig. S1 in Supplementary material shows the different architectures obtained). Moreover, the SiO₂ layer prevents the diffusion of Na⁺ cations from the glass substrate

to the TiO₂ coating during firing and the possible inhibition of photo-catalytic activity.

SiO₂ and Ag-doped SiO₂ layers were deposited at 25 and 35 cm/min, respectively, and heat-treated at 450 °C for 30 min. On the other hand, dense and mesoporous TiO₂ layers were deposited using the Ag-doped and undoped TiO₂ and TiO₂-Brij58 sols at 25 and 35 cm/min respectively, at 20% RH. The TiO₂ coating was heat-treated at 450 °C for 1 h with a heating rate of 10 °C/min. Thus, all the slides were coated on both sides with a total area of 25 cm².

2.2. Characterization of coatings

Thickness (e) and refraction index (n) were measured using a Spectroscopic Ellipsometer (WVASE32, “Variable Angle Spectroscopic Ellipsometer” J.A. Co., Woollam M-2000UTM). The pore volume of the films was determined, using the Bruggeman Effective Medium Approximation (BEMA), and considering a non-doped SiO₂ coating and a dense TiO₂ coating as near-dense reference materials.

TEM images of the Ag-doped layers were obtained by scratching the films and depositing the scaled fragments onto carbon-coated copper grid. TEM images were obtained after complete solvent evaporation.

GXRD patterns of Ag-doped SiO₂ and Ag-doped dense and mesoporous TiO₂ monolayers deposited onto Si-wafers were obtained in a PANalytical diffractometer (X'Pert PRO theta/theta), with CuK_α radiation, an incidence angle of 0.5°, an increment of 0.05°, and a counting time of 20 s/step.

UV–vis absorption spectra of Ag-doped and no-doped SiO₂ and TiO₂ monolayers deposited on quartz were recorded using Jasco V-530 equipment at room temperature in the range of 200–1100 nm. Band gap values were determined using the Eq. (1).

$$(\alpha E)^{1/m} = A(E - E_g) \quad (1)$$

where α is the absorption coefficient, E is the energy of the incident photon, E_g is the band gap energy, A is a constant, and m is a parameter that depends on the electronic transition of the semiconductor; for indirect transition semiconductor such as TiO₂-anatase phase $m = 2$ [57].

Photoluminescence emission spectra (PL) of photocatalytic samples were performed to take light on the mechanism of photo-assisted reactions. Spectra were recorded by a Shimadzu RF-5301PC spectrofluorophotometer with a Xe lamp adjusting the excitation wavelength at 280 nm.

2.3. Photocatalytic tests

Photocatalytic performance was evaluated through the degradation of methyl orange in an aqueous solution. Four coatings were immersed in 50 mL of a methyl orange solution at pH = 2. The container was covered with window-glass to avoid evaporation. The system was irradiated from the top with three 6 W UV lamps with maximum emission at 365 nm (Philips F/TL/6 W/08, Holland). Methyl orange degradation was followed by UV–vis spectroscopy measuring the variation of the band intensity at 508 nm with time up to 150 min. The complete process is described in [56]. The kinetic parameter and the half-life have been calculated from experimental data and are included in Table 1 to allow discussion on photocatalytic activity. Reference runs were conducted with samples and with no light activation (adsorption) and with light in the absence of sample film semiconductor (photolysis).

Table 1
Characteristics and properties of multilayer coatings.

Sample name	Coating composition	Thickness (nm)	Pore volume (%)	Kinetic parameters of photocatalysis		[Ag ⁺] released (μg/L)
				k (min ⁻¹)	t _{1/2} (min)	
Ag-SiO ₂	Ag-doped SiO ₂	380	7	–	–	415
SiO ₂ /TiO ₂ dense	SiO ₂	210	–	0.0056	123	0
	TiO ₂ dense	90	–	–	–	–
Ag-SiO ₂ /TiO ₂ dense	Ag-doped SiO ₂	380	7	0.0124	56	70
	TiO ₂ dense	170	–	–	–	–
SiO ₂ /Ag-TiO ₂ dense	SiO ₂	210	–	0.0084	82	1081
	Ag-doped TiO ₂ dense	290	12	–	–	–
SiO ₂ /TiO ₂ meso	SiO ₂	210	–	0.0071	97	0
	TiO ₂ -meso	140	25	–	–	–
Ag-SiO ₂ /TiO ₂ meso	Ag-doped SiO ₂	380	7	0.0178	39	43
	TiO ₂ -meso	280	25	–	–	–
SiO ₂ /Ag-TiO ₂ meso	SiO ₂	210	–	0.0138	50	1287
	Ag-doped TiO ₂ meso	300	29	–	–	–

2.4. Bacterial strains, antibacterial test and growth conditions

Four different bacterial species were used to test the antimicrobial activity of the coatings against planktonic forms and spores. Two strains were representative of spore-forming pathogenic bacteria: Sterne strain 34F2 and strain SM101, models of anthrax-producer *B. anthracis* and enterotoxin-positive and gas-gangrene producing *C. perfringens* pathogens, respectively [45,46,48,49,51]. The two remaining strains, spore-deficient, but pathogenic for humans, used in this work were the hemolysin-positive *L. monocytogenes* strain ATCC 7644 [20] and the ampicillin-resistant enterohemorrhagic *E. coli* (EHEC) strain O157:H7 [26]. *B. anthracis* and *C. perfringens* were grown in the BHI (Brain Heart Infusion) medium under aerobic and anaerobic conditions, respectively, to recover the vegetative forms of each bacterium [48,50]. Alternatively, *B. anthracis* cells were grown in the Schaeffer's sporulation medium (SM) under aerobic conditions at 37 °C [48,58,59] and *C. perfringens* was grown in the Duncan Strong sporulation medium (DSSM) under anaerobic conditions at 37 °C (Oxoid Anaero-systems) [45,46]. The growth of *B. anthracis* and *C. perfringens* in SM and DSSM media, respectively, allowed the obtaining of a high titer of spores of each bacterium. Enterohemorrhagic *E. coli* (EHEC) was grown in Luria-Bertani broth (LB, Difco Co.) [27,60] and *L. monocytogenes* was grown in Trypticase Soy Broth (TSB, Oxoid Co.) [20].

2.5. bactericidal and sporocidal activity assays

The glass slides holding the different composites were washed and sanitized five times with water and ethanol before use [43,44] and were located in moisture chambers (Petri dishes with moist filter paper on the bottom). Fifty microliters containing an average number of 1×10^6 CFU of stationary-phase cultures of cells of *E. coli* or *L. monocytogenes* was placed on top of each slide in triplicate. In the case of *B. anthracis* and *C. perfringens*, 1.0 mL of stationary phase cultures of each strain was heated at 80 °C for 20 min (to kill vegetative cells) and treated with lysozyme ($3.0 \text{ mg} \cdot \text{mL}^{-1}$) for 1 h at 37 °C, in order to lyse the dead vegetative cells (spores are fully resistant to heat and lysozyme treatments) [34,48]. After the hydrolysis of the dead vegetative cells, the remaining cells (viable spores) were washed three times with cold water, centrifuged and finally resuspended in 1.0 mL of PBS buffer before use. After this treatment, the samples contained 100% pure spore cells (as evaluated by phase contrast microscopy and cell

count before and after heating) at an average concentration of 2×10^9 spores/mL⁻¹. These spore samples were concentrated (by centrifugation) as needed in order to reach the titer of spores (average of 1×10^{10} spores) used for each treatment.

The glass composites containing the different bacteria were then irradiated with a black-light UV lamp, 365 nm, for different time periods (from 15 min to 9 h exposure at 15 min intervals). After the various time-exposure tests, we selected exposure times of 45 min for vegetative (planktonic) cells and of 2 h for spore cells, as these times provided reproducible and comparable biocidal effects between the tested strains under the different exposure conditions. After the irradiation periods, the bacterial droplets were swabbed from the slides under sterile conditions, transferred to sterile test tubes containing 5 mL of water and vortexed to dissolve the cells. For a qualitative analysis of the bactericidal effect on planktonic cells, we used the LIVE/DEAD BacLight Bacterial Viability Kit from Invitrogen Co. (under the fluorescence microscope, viable cells are green and dead cells are red). Cells were observed by phase contrast and fluorescence microscopy and photographed using an Axiostar Plus microscope (Carl Zeiss, Inc.) equipped with an epi-fluorescence attachment and a digital camera system (Canon Power Shot A-620) [45,58]. The ImageJ software package was used for camera control and image processing [45,58]. For a quantitative analysis of the bactericidal effect, serial 10-fold dilutions of the non-sporulating bacterial suspensions (*E. coli* and *L. monocytogenes*) were prepared, after treatments, in sterile water and plated in agarized (2% Difco Bacto agar) media (LB and TSB, respectively). For the spore-formers (*B. anthracis* and *C. perfringens*), serial ten-fold dilutions were plated in duplicate before (viable cell count) and after heat treatment at 80 °C during 20 min (spore count). Viable cells and spores were grown O/N at 30 °C in BHI agar plates under aerobic (*B. anthracis*), or anaerobic (*C. perfringens*) conditions before cell counting. The surviving bacteria were counted as CFU (Colony Forming Units) per milliliter, and the mean values were indicated as described [60].

2.6. Measurement of silver ion release

Silver ion release from Ag-doped coatings to an aqueous medium in direct contact was measured by anodic stripping voltammetry (ASV). One coating of each sample was immersed in 50 mL of 0.01 M HNO₃ with magnetic stirring. HNO₃ was added to protect the released Ag⁺ ions from reducing to metallic silver [15]. After 45 min, an aliquot of 5 mL was acquired to quantify the Ag⁺ ion concentration.

Quantitation of silver ions released was carried out by the ASV technique. The methodology was chosen because it is accomplished using a bulk pre-electrolysis step, that allows concentrating of silver on the surface of the electrode. Afterwards, the analyte is electrochemically dissolved, and a signal-to-noise ratio higher than with conventional electrochemical techniques is reached, therefore enhancing the sensitivity. This is an essential point because very low silver ion concentrations can be determined. All the reagents used for electrochemical determinations were of the highest analytical grade quality, and solutions were prepared in high purity MilliQ® water. Experiments were performed using an Autolab-Eco Chemie electrochemical analyzer, equipped with PGSTAT 30 software. The cell was a conventional three-electrode one, with a glassy carbon rotating disk electrode as the working electrode, and a glassy carbon rod as the counter electrode. A double-junction KNO₃ (3 M) KCl (3 M), Ag AgCl was used as a reference electrode. Before the first analysis, the working electrode was polished with aluminum oxide powder (grain size 0.3 μm), thoroughly rinsed with MilliQ® water, and preconditioned by immersing it for 10 min in HNO₃ (1:1 volume-to-volume), and finally was rinsed again with MilliQ® water. To perform the electrochemical experiments, 5.00 mL of the sample properly diluted (1/20 to 1/2 volume-to-volume in 0.01 M HNO₃, depending on sample concentration) was added into 10.00 mL 0.2 M KNO₃, 0.004 M EDTA supporting electrolyte, to register the voltammogram as the average

of 2 consecutive scans. The sample concentration was determined using the standard addition method, according to the following protocol: 0.025 mL of standard solution (10 mg L⁻¹ Ag⁺ in 0.01 M HNO₃) was added into the cell with the previously analyzed sample, to register a new voltammogram (2 scans averaged) and, subsequently, additional 0.025 mL of standard Ag⁺ solution was added to register the new voltammogram. All concentrations are informed as the average of 2 independent replicate determinations with a relative error of about 2%. The electrochemical experiments were performed by differential pulse ASV, under the following conditions: working electrode rotation speed, 2000 rpm; purge time, 300 s; pulse amplitude, 0.050 V; cleaning potential, 0.45 V; cleaning time, 60 s; deposition potential, -0.4 V; deposition time, 120 s; equilibration time, 5 s; start potential, 0 V; end potential, 0.45 V; voltage step, 4 mV; voltage step time, 0.1 s; and sweep rate, 0.040 V s⁻¹.

3. Results and discussion

3.1. Obtention and characterization of coatings

First, Ag NPs were obtained by the colloidal technique in ethanol and by stabilizing with organic compounds. ATS stabilized silver nanoparticles (AgATS) were obtained as spherical particles with a mean diameter of 17 ± 4 nm, as shown in Fig. 1A, whereas PVP stabilized nanoparticles (AgPVP) were spherical with a mean size of 7 ± 2 nm with a few bigger particles between 20 and 40 nm diameters (Fig. 1B). The silver

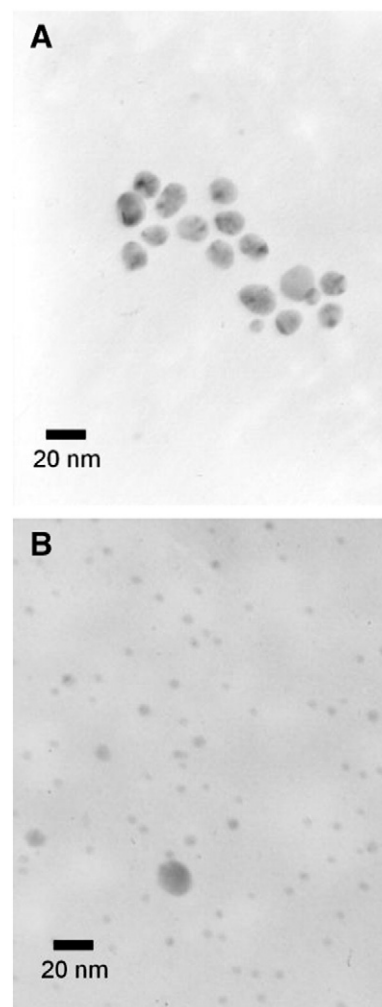


Fig. 1. TEM images of silver nanoparticles: A) ATS-stabilized nanoparticles and B) PVP-stabilized nanoparticles.

nanoparticles have sizes in the range of the plasmonic effect, i.e., between 2 and 50 nm, according to the literature [61].

Ag-doped sol-gel precursors were obtained by adding colloidal silver nanoparticles to SiO₂ or TiO₂ sols. Then, transparent and homogeneous Ag-doped and no-doped SiO₂ and TiO₂ films were obtained by immersion from the described sols. The values of thickness and volume pore obtained from ellipsometric data are listed in Table 1.

TEM image of Ag-SiO₂ film is shown in Fig. 2A; the heat-treatment temperature is lower than the melting point of these nanoparticles [62], thus they maintained their properties during the entire process. On the other hand, Ag nanoparticles were partially degraded in the Ag-TiO₂ films obtaining; likewise, some Ag nanoparticles maintained their identity, especially in mesoporous film, favored in this latter case by the reducing effect of the surfactant [63]. TEM images (Fig. 2) show that the mean size of silver nanoparticles remains almost unchanged within the range of the plasmonic effect. By GXRD amorphous SiO₂, TiO₂ anatase phase and Ag-fcc structures were identified. GXRD patterns are insets in Fig. 2A, B and C. The main diffraction peaks from Ag-fcc (JCPDS 04-0783) are observed at $2\theta = 38.15$ (111) and 44.3 (200). In GXRD of Ag-doped TiO₂ layers the main peak of Ag fcc at 38.15 overlaps the diffraction peak at $2\theta = 38.1$ corresponding to (004) plane of anatase TiO₂ (JCPDS 21-1272). In the GXRD of the dense Ag-TiO₂ layer (Fig. 2B) an additional peak appears centered at $2\theta = 46.3$ and it is attributed to AgCl (JCPDS 31-1238) that results from the partial oxidation of Ag nanoparticles to Ag⁺ ions and their combination with Cl⁻ from the HCl used as catalyst for sol-gel reactions. Thus, GXRD data of Ag-doped dense and mesoporous TiO₂ samples clearly shows that the surfactant Brij-58 retains the metallic silver nanoparticle state.

To study the optical properties of the films, monolayer coatings were deposited onto vitreous silica substrates and analyzed by UV-vis spectroscopy. Experimental results are represented as $(\alpha E)^{1/2}$ vs E in Fig. 3.

The E_g can be calculated through Eq. (1) by fitting the linear relation of $(\alpha E)^{1/2}$ versus E plot. The calculated E_g were: 3.50 ± 0.05 eV for the dense TiO₂ layer, 3.57 ± 0.05 eV for the dense Ag-TiO₂ layer, and 3.60 ± 0.05 eV for mesoporous TiO₂ and Ag-TiO₂ layers. All these values are higher compared to E_g of bulk TiO₂ (3.2 eV). This shift might be associated to the small crystallite size of TiO₂ in the films (between 7 and 17 nm) which strongly affects the band-gap due to quantum confinement effect [64]. Also, the increase of porosity shifts the band-gap to higher energies [63], as could be observed from the comparison of E_g calculated values for dense (3.50 ± 0.05 eV) and mesoporous (3.60 ± 0.05 eV) TiO₂ layers. On the other hand, some authors showed that the band gap energy might shift to lower energy associated with the Ag loading [65]. However, this latter effect was not registered for the Ag-doped samples. The band gap

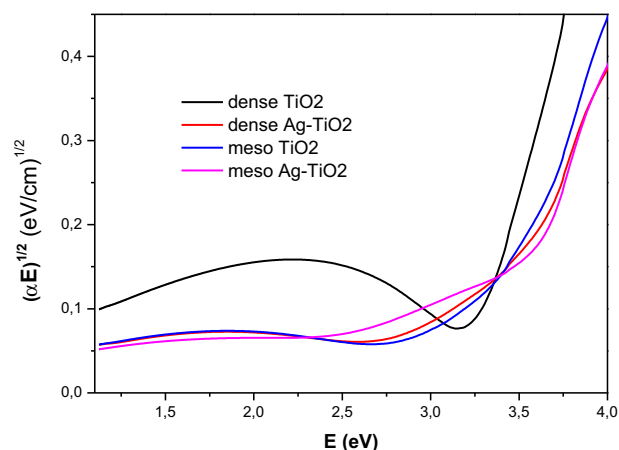


Fig. 3. $(\alpha E)^{1/2}$ vs E graphics obtained from to apply Eq. (1) to UV-vis transmission spectra of Ag-doped and no-doped TiO₂ coatings onto SiO₂.

energy values calculated from the corresponding UV-vis spectra were nearly the same for both mesoporous samples (3.60 ± 0.05 eV). Moreover, the E_g increased by Ag-doping of the dense TiO₂ layer (from 3.50 ± 0.05 to 3.57 ± 0.05 eV) and this behavior is attributed to the increase in porosity. The photocatalytic process begins with the irradiation of the material by UV light with energy higher than the band gap energy. The absorption process in the semiconductor generates energetic electron-hole (e-h) pairs which are involved in the catalytic reactions. The behavior of these photogenerated species was studied through photoluminescence (PL) measurements of photocatalytic multilayer mesoporous coatings (Fig. 4). The PL is observed when the e-h pairs recombine at some defect-related centers (oxygen vacancies at the grain boundaries of the polycrystalline TiO₂ layer) and then, the relaxation of system occurs with the loss of energy as light emission originating the emission peaks [66].

A broad emission band between 380 and 490 nm is observed in the PL emission spectrum of the mesoporous SiO₂/TiO₂ coating (Fig. 4). Several well resolved peaks can be identified which are assigned to electronic transitions that involve different energy levels [66]. The PL emission spectrum of mesoporous Ag-SiO₂/TiO₂ coating shows a lower intensity than the corresponding undoped sample, probably due to silver nanoparticles located in the interface between SiO₂ and TiO₂, allowing direct contact with the TiO₂. Since PL emission occurs when the electron-hole pairs are recombined, the decrease of PL intensity for Ag-doped samples indicates that there is a partial inhibition of the e-h recombination process [67,68] which can be attributed to the

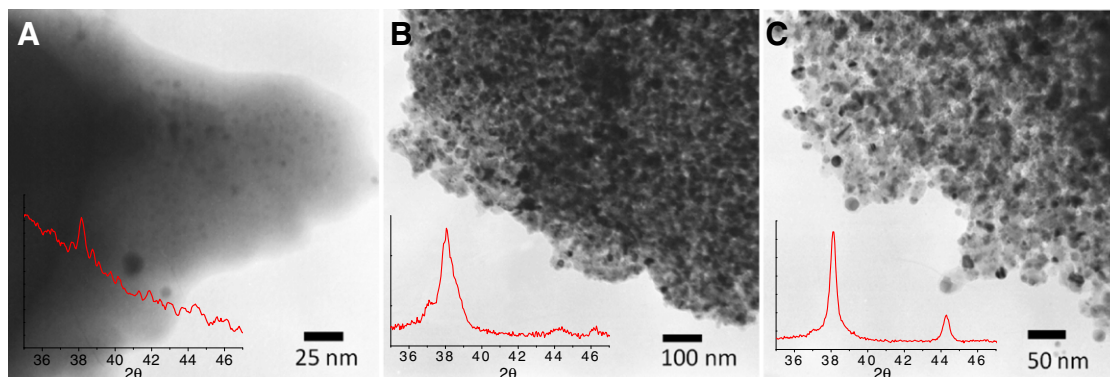


Fig. 2. TEM images of Ag-doped films: A) Ag-SiO₂ layer, B) dense Ag-TiO₂ layer and C) mesoporous Ag-TiO₂ layer, inset) GXRD patterns of the corresponding Ag-doped monolayer onto Si-wafer.

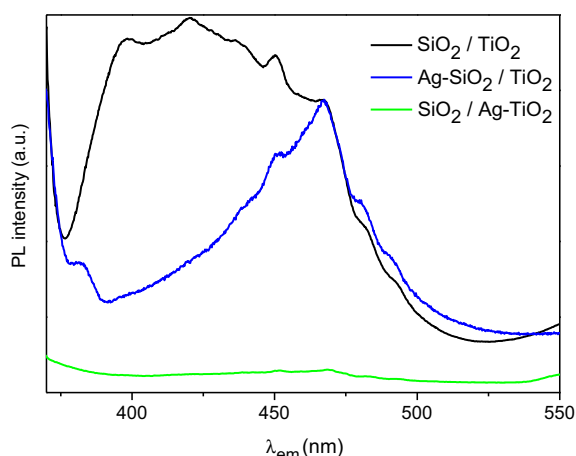


Fig. 4. PL spectra of mesoporous samples: $\text{SiO}_2\text{-TiO}_2$, $\text{Ag-SiO}_2/\text{TiO}_2$ and $\text{SiO}_2/\text{Ag-TiO}_2$.

interaction between silver nanoparticles and TiO_2 . The energetic electrons photogenerated in TiO_2 can be transferred to silver nanoparticles, and so, the e–h recombination process is delayed. The presence of Ag NPs in the interface seems to be enough to cause the delay of the e–h recombination and the consequent PL intensity decrease.

In the PL spectrum of mesoporous $\text{SiO}_2/\text{Ag-TiO}_2$ sample a total extinction of the PL is observed. Again, the energetic electrons are transferred from TiO_2 to Ag NPs, and then, the recombination process is delayed and consequently PL decreases. This effect is higher in Ag-doped samples in the TiO_2 layer than in those doped in the SiO_2 layer; this supports the idea of the effect of direct contact between TiO_2 and Ag NPs. The same behavior is observed in dense films (not shown).

3.2. Photocatalytic behavior of the systems

The photocatalytic activity was studied through the degradation of methyl orange (MO) in aqueous solution under the UV illumination of Ag-doped and no-doped SiO_2 and TiO_2 films onto glass-slides. The preliminary tests showed that neither photolysis nor adsorption processes occur, thereby all the degradation of MO observed is associated only with the photocatalytic effect of samples.

In the case of Ag-SiO_2 coating, the photocatalytic activity is negligible, indicating that Ag NPs embedded in the SiO_2 matrix are not photocatalytically active.

The kinetic parameters of the photocatalytic decomposition of MO by the photoactive samples were calculated from experimental data following a first order kinetic model, $\ln(C_0/C) = kt$, where C_0 and C is the concentration at $t = 0$ and at time t , respectively. The first order rate constants, k , together with the $t_{1/2}$ (time for half concentration) for the different multilayer coatings are shown in Table 1.

The k parameters of $\text{Ag-SiO}_2/\text{TiO}_2$ meso, $\text{SiO}_2/\text{Ag-TiO}_2$ meso and $\text{Ag-SiO}_2/\text{TiO}_2$ dense were the highest, indicating faster degradation rate than other samples. The most active photocatalyst with $t_{1/2}$ of 39 min and $k = 0.0178 \text{ min}^{-1}$ was the $\text{Ag-SiO}_2/\text{TiO}_2$ meso sample, followed by $\text{SiO}_2/\text{Ag-TiO}_2$ meso ($k = 0.0138 \text{ min}^{-1}$, $t_{1/2} = 50 \text{ min}$) and $\text{Ag-SiO}_2/\text{TiO}_2$ dense ($k = 0.0124 \text{ min}^{-1}$, $t_{1/2} = 56 \text{ min}$).

Several mechanisms may act on the reinforcement of photocatalytic activity: 1) increase of the contact surface between the catalytic material and the reaction medium [56], 2) increase of the optical length through TiO_2 by dispersion effects from NPs [69], 3) decrease of E_g by Ag-doping of TiO_2 [65], 4) increase of concentration of energetic reactive species by delaying the e–h recombination [67], and 5) increase of light intensity by local surface plasmon resonance and reinforcement of the near electric field [70].

To investigate the influence of the first mechanism, similar samples with and without porosity have been compared. In all cases, mesoporous coatings showed a higher photocatalytic efficacy than dense samples. The porosity in the TiO_2 layer improved the photocatalytic behavior because the specific surface area increases and enhances the contact between the catalytic material and the pollutant [56].

The second mechanism is based on the increase of the optical length by dispersion from the silver nanoparticles in the TiO_2 layer. A slight decrease of the transmittance to short wavelength (mainly below 440 nm) is observed in the respective UV–vis transmittance spectra of Ag-doped TiO_2 layers, but this effect is attributed to the increase of roughness. Thus, there is no evidence that this mechanism would contribute to photocatalysis enhancement.

The third mechanism is related to E_g decrease by doping TiO_2 with silver nanoparticles. Several authors showed that the incorporation of small amounts of metal nanoparticles can extend the band gap energy of TiO_2 to the visible region and modify the photocatalytic properties [65]. However, in our case the Ag NP doping does not change the band gap indicating that this mechanism could not explain the different behaviors observed between the doping and un-doping samples.

The fourth mechanism acts when silver nanoparticles and TiO_2 are in direct contact. This mechanism is initiated with the transfer of the photoexcited electron from TiO_2 to Ag NPs. Then, the separation of electron and holes is favored and the recombination is delayed, increasing the concentration of the reactive species. PL measurements (Fig. 4) showed that this mechanism occurs in $\text{SiO}_2/\text{Ag-TiO}_2$ samples, whereas it takes place with lower intensity in $\text{Ag-SiO}_2/\text{TiO}_2$ samples since only the particles on the top of the SiO_2 layer (interface) are in direct contact with TiO_2 .

The last possible mechanism [70] involves the excitation of the local surface plasmon resonance (LSPR) of silver nanoparticles. When the LSPR is excited, a strong electric field is produced around the nanostructure whose order of magnitude is higher than the field of incident photons. As the e–h pair formation rate in semiconductors is proportional to the local intensity of the electric field, the concentration of reactive species will increase with the electric field [69] and thus will enhance the photocatalytic activity. This mechanism may occur even if silver nanoparticles and TiO_2 are not in direct contact, even at dozens of nanometers [69,70] as in the interface between the Ag-SiO_2 and TiO_2 layers. Thus, the contribution of this mechanism could explain the better photocatalytic activity of $\text{Ag-SiO}_2/\text{TiO}_2$ samples compared to $\text{SiO}_2/\text{Ag-TiO}_2$ samples. It is worth noting that the occurrence of this mechanism is usually accepted as an explanation of the enhancement of the photocatalytic activity of semiconductors by metal nanoparticles [69] supported by experimental data [71] and in agreement with theoretical analysis [70]. Also, silver nanoparticles used for doping are spheres with sizes in the range of the plasmonic effect [61]. From these issues, this mechanism is considered suitable to explain the photocatalytic behavior.

In conclusion, the highest photocatalytic activity is obtained for $\text{Ag-SiO}_2/\text{TiO}_2$ meso coating associated with the porosity of the mesoporous coatings, the increase of the electric field related with the SPR effect, and also the increase in the concentration of energetic reactive species by delaying the e–h recombination. The next efficient photocatalyst is $\text{Ag-SiO}_2/\text{TiO}_2$ dense coating, because the contact area with the medium is smaller than for $\text{Ag-SiO}_2/\text{TiO}_2$ meso coating, whereas the other enhancement mechanisms are the same. Finally, $\text{SiO}_2/\text{Ag-TiO}_2$ samples (meso and dense respectively) are less photocatalytic because there is a partial degradation of Ag nanoparticles during the Ag-TiO_2 layer preparation; thus, $\text{Ag-SiO}_2/\text{TiO}_2$ samples have a higher loading of silver nanoparticles.

All the coatings studied here have a good performance as photocatalysts and they are able to break organic compounds. As these coatings avoid the deposition of proteins on the surface and then hinder the adherence of bacteria, they contribute indirectly to the microbicidal properties.

3.3. Antimicrobial activity of multilayer systems

The microbicidal activity of the coatings was assayed against four human-pathogenic bacterial species that were selected for their medical relevance and their negative socio-economic impact [18,19,47,51]: the Gram-negative ampicillin-resistant enterohemorrhagic *E. coli*, EHEC [24,28]; the Gram-positive hemolysin-positive *L. monocytogenes* [20–23], and two spore-formers, *B. anthracis* and *C. perfringens* [45–51].

Under light-irradiation, all Ag-doped SiO₂ and TiO₂ coatings produced a reproducible and evident bactericidal effect on EHEC and

L. monocytogenes cells, although to different degrees. Fig. 5 shows the survival rates of both pathogens after their exposure to the different coatings.

It can be seen that the single treatments with Ag (Ag–SiO₂) and TiO₂ (SiO₂/TiO₂ dense and mesoporous) were bactericidal against EHEC and *L. monocytogenes* cells (Fig. 5A and B, respectively). The survival rates of EHEC after expositions to Ag–SiO₂ and SiO₂/TiO₂ (dense and mesoporous) coatings were of 50% and 30% respectively (Fig. 5A). This bactericidal effect was significantly enhanced when Ag NPs were embedded to SiO₂/TiO₂ coatings. In this case, the survival rates dropped to 20–25%

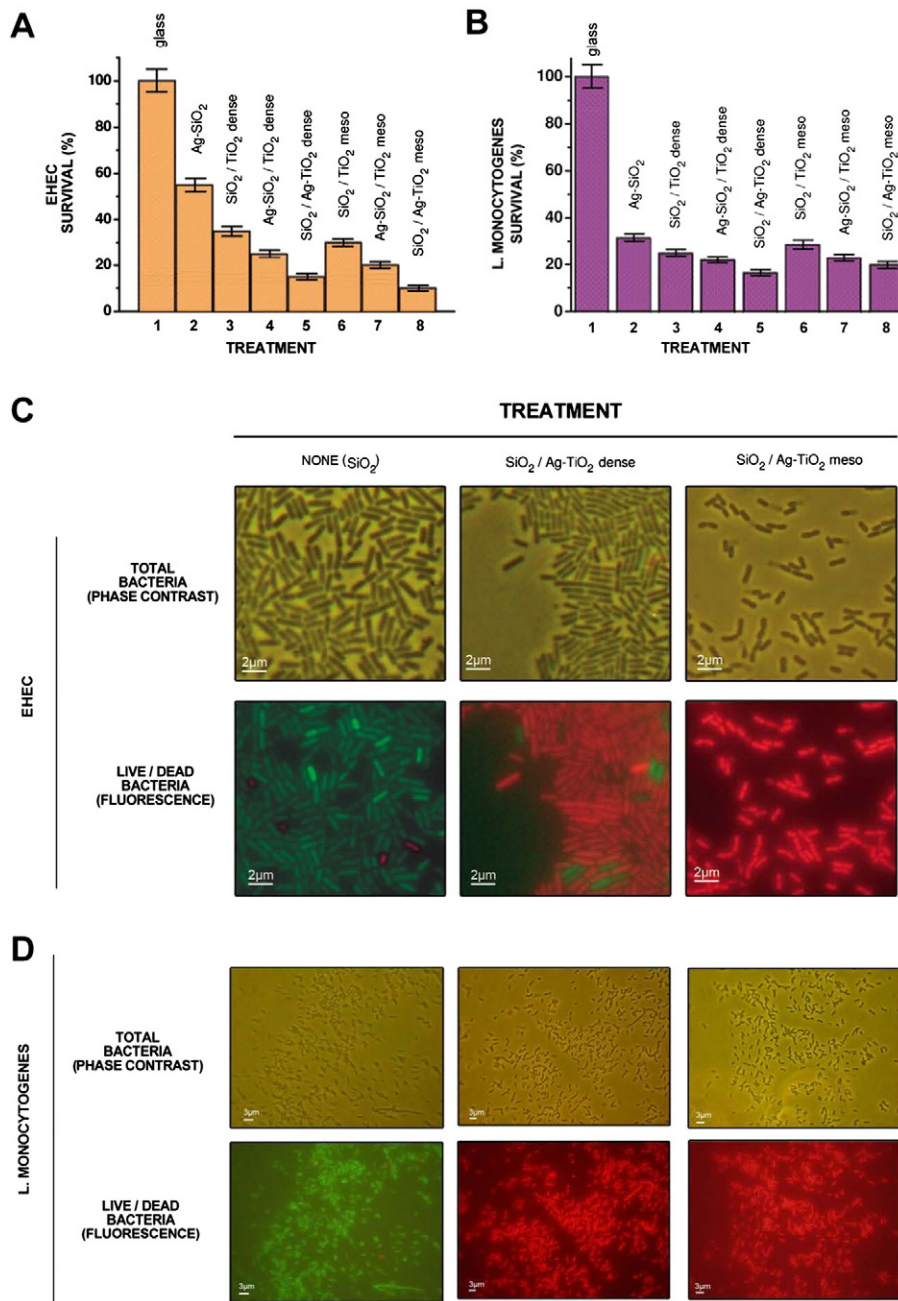


Fig. 5. Bactericidal activity of Ag and/or TiO₂ films against Gram-negative and Gram-positive bacteria under UV irradiation. (A–B) Percentage of EHEC (A) or *L. monocytogenes* (B) survival. Viable cells were counted as CFU per milliliter. The mean values of three independent experiments are shown. The error bars represent standard errors. The number of viable cells (EHEC or *L. monocytogenes*) recovered from no-coated glass slides kept in a dark environment or after 45 min of irradiation did not differ significantly from one another (9×10^5 to 1×10^6 recovered viable cells per glass slice treatment) and correspond to 100% survival. (C–D) Phase contrast and fluorescent microscopy of EHEC (C) and *L. monocytogenes* (D) cells before and after treatments with SiO₂/Ag–TiO₂ composites. After the irradiation periods, three independent bacterial droplets from treatments 1, 5 and 8 showed in (A and B) were swabbed from the slides, transferred to sterile test tubes containing 5 mL of water and vortexed to dissolve the cells. Twenty microliters of each cell resuspension was observed by phase contrast (total bacteria, live plus dead) and fluorescence microscopy using an Axiostar Plus microscope. In (C–D) viable cells are green and dead cells are red. The resulting photographs of a representative experiment from three replications are shown and indicate that more than 90% of initial viable EHEC and *L. monocytogenes* cells were killed after the treatment with SiO₂/Ag–TiO₂ films.

when Ag was first embedded into the SiO₂ layer and then coated with TiO₂ (Ag–SiO₂/TiO₂ dense or mesoporous). On the other hand, the bactericidal effect was the highest when Ag was enclosed into the TiO₂ layer, either dense or mesoporous. Under these conditions the survival of EHEC cells dropped to less than 15%. It is interesting to note that SiO₂/Ag–TiO₂, either dense or meso, (bars 5 and 8 in Fig. 5A, respectively) has a higher bactericidal effect than Ag–SiO₂/TiO₂, either dense or mesoporous (bars 4 and 7 in Fig. 5A, respectively), suggesting that it is important that Ag NPs and TiO₂ are enclosed together. In the case of *L. monocytogenes* (Fig. 5B), this pathogen was more sensitive than EHEC to single treatments with Ag or TiO₂, either dense and mesoporous. The best microbicidal results were obtained, again, with SiO₂/Ag–TiO₂ dense and mesoporous coatings (20% to 15% survival, Fig. 5B).

To confirm the high bactericidal effect of the SiO₂/Ag–TiO₂ coatings, the cell survival rate was analyzed using an approach different from cell counting. To this end, a vital live/dead fluorescent assay was used [45, 58]. In this system, two different nucleic acid stains were used to distinguish rapidly between viable cells with intact membranes and functional metabolism (green fluorescence) from dead or damaged cells with compromised membrane integrity (red fluorescence) [45, 58]. As a confirmation for the above CFU counting results, both biocidal treatments (SiO₂/Ag–TiO₂ dense and SiO₂/Ag–TiO₂ mesoporous, bars 5 and 8 in Fig. 5A–B, respectively) yielded more than 90% of dead or severely damaged EHEC and *L. monocytogenes* cells, Fig. 5C and D, respectively.

The susceptibility of EHEC and *L. monocytogenes* (typical Gram-negative and Gram-positive pathogenic bacteria, respectively) was higher for Ag-doped SiO₂/TiO₂ films compared with undoped SiO₂/TiO₂ materials. These results suggest that the thick, but solute-permeable, peptidoglycan layer of *L. monocytogenes* and the periplasmic space and outer membrane of EHEC do not represent efficient permeability barriers to the diffusion of hydroxyl radicals from TiO₂ and silver ions (Ag⁺) released by Ag nanoparticles. In addition, the higher susceptibility of *L. monocytogenes* with respect to EHEC might reflect the nature of the higher permeability of a Gram-positive cell wall compared to the lower permeability of a Gram-negative cell wall due to the presence, in the latter, of the lipopolysaccharide-containing external membrane [18,19,59]. It is believed that the bactericidal effect of TiO₂ and Ag NPs on typical Gram-positive and Gram-negative bacteria is shared and universal among bacteria. Although it is hard to separate and distinguish the bactericidal effect of Ag NPs from that of the released ions, the global bactericidal effect is unspecific and mainly due to the cumulative action of released hydroxyl radicals and Ag⁺ on the stability and the activity of bacterial proteins (mainly membrane-associated proteins involved in the electron transport chain), plus the interference with the transcriptional and translational-protein synthesis machineries of the bacteria [7,12,29–32]. The disturbance of the cell wall plus the disruption of the electron transport chain cause a collapse of the proton motive force that blocks most of the membrane-associated processes such as transport processes across the membrane, flagella-mediated bacterial motility and synthesis of ATP. In addition, the damages produced on the bacterial nucleoid (for example, DNA mutations) and the inhibition of the de novo protein synthesis due to the damage and the interference of the ribosome functions altogether lead to the irreversible inactivation and death of the microbe [7,12,29–32].

Besides the clinical and socio-economical relevance of the two analyzed pathogens (EHEC and *L. monocytogenes*), bacterial spores are tremendously resistant and represent the most persistent form of bacteria in nature [34,48]. Spores formed by pathogenic bacteria (mainly from pathogenic Bacilli and Clostridia) represent the most dangerous and threatening infective agents to human health. Even though their clinical relevance, few reports have informed about the susceptibility of bacterial spores to materials containing TiO₂ and/or Ag NPs alone or

in combination. The susceptibility of *B. subtilis*, *B. anthracis* and *B. cereus* spores to TiO₂ adducted with halogen, silver, carbon, sulfur and carbon nanotubes [39,41,42] or silver and copper nanoparticles alone [37] has been reported. In the case of Clostridia, *C. difficile* and *C. botulinum* spores were treated with metal oxides (TiO₂ and AgO, respectively) alone [40,43]. However, to our best knowledge, there is only one report about the susceptibility of a pure suspension of pathogenic spores (*B. cereus* spores) to the contact with Ag nanoparticles embedded in TiO₂ materials [44]. Therefore, we consider that the analysis of the susceptibility of other types of pathogenic spores (*B. anthracis* and *C. perfringens*) to our developed composites will be interesting and important.

Fig. 6A shows the survival percentage of an initial high number of viable pathogenic spores from *B. anthracis* (initial number of 3×10^{10} spores/composite) and *C. perfringens* (initial number of 8×10^9 spores/composite) after contact with SiO₂/Ag–TiO₂ dense and SiO₂/Ag–TiO₂ mesoporous coatings that previously showed the highest microbicidal effects against planktonic bacteria (see Fig. 5). Interestingly, both types of composites yielded similar high values of sporocidal activity against *B. anthracis* and *C. perfringens* spores (70% and 90% mortality, respectively). As expected, the germination ability of the treated-spores (Fig. 6B) was severely impaired, pointing out the potential use of Ag-doped TiO₂ films to prevent spore germination and the subsequent blockage of the development of spore-linked human diseases due to the accidental or intentional release (e.g., in bioterrorist acts) of pathogenic spores. To our best knowledge, this is the first time that the germicidal effect of Ag-doped TiO₂ films on suspensions containing 100% of pure *B. anthracis* and *C. perfringens* pathogenic spores is shown.

Compared to the susceptibility of planktonic cells, bacterial spores were, as expected, more resistant to the contact with Ag-doped TiO₂ composites and needed more time of exposure (2 h versus 45 min of exposure for spores and planktonic cells, respectively) to get similar results of bacterial inactivation. In fact, while the exposure to the Ag-doped TiO₂ composites kill 100% of the planktonic forms of EHEC and *L. monocytogenes* after 90 min of treatment, the same type of treatment and exposure time for *B. anthracis* and *C. perfringens* spores eliminated no more than 10% of the viable spores (data not shown). The spores are highly resistant to several germicidal compounds and difficult to eliminate because of their structure and chemical composition. This is mainly due to the detoxifying activity of specific proteins present in the spore coat (i.e. superoxide dismutase, SOD); the dipicolinic acid (DPA) present in the spore cortex that is important for the dehydration of the spore cytosol; the rigid inner membrane of the spore that is responsible for its remarkable impermeability; the dehydrated spore core (cytosol) responsible for chemical resistance; and finally, the presence of small acid-soluble proteins (SASPs) that minimize the effects of radiation on the spore DNA [34,48,49].

The vegetative (planktonic) bacteria and spores studied here resulted more susceptible to the SiO₂/Ag–TiO₂ (dense or meso) coatings. To understand the origin of this behavior Ag⁺ ions released to the medium were quantified by voltammetric measurements. Fig. 7 shows a typical voltammogram and the inset displays the regression line obtained for the standard addition procedure of one sample analysis. At the 45 minute timepoint, Ag–SiO₂/TiO₂ dense samples released 70 µg/L of Ag⁺ ions, whereas SiO₂/Ag–TiO₂ samples released 1081 µg/L. The same behavior was observed in mesoporous samples (Table 1). Thus, samples doped with AgPVP nanoparticles (diameter = 7 ± 2 nm) in the outer TiO₂ layer released a higher concentration of bactericidal Ag⁺ ions than samples doped with AgATS nanoparticles (diameter = 17 ± 4 nm) in the inner SiO₂ layer and this fact explains the better bactericidal effect of the first ones. Two aspects of SiO₂/Ag–TiO₂ sample architecture contribute to increase the Ag⁺ release rate with respect to Ag–SiO₂/TiO₂ samples: 1) the mean size of Ag nanoparticles, and 2) the exposure of the doped layer to the medium. SiO₂/Ag–TiO₂ dense and mesoporous

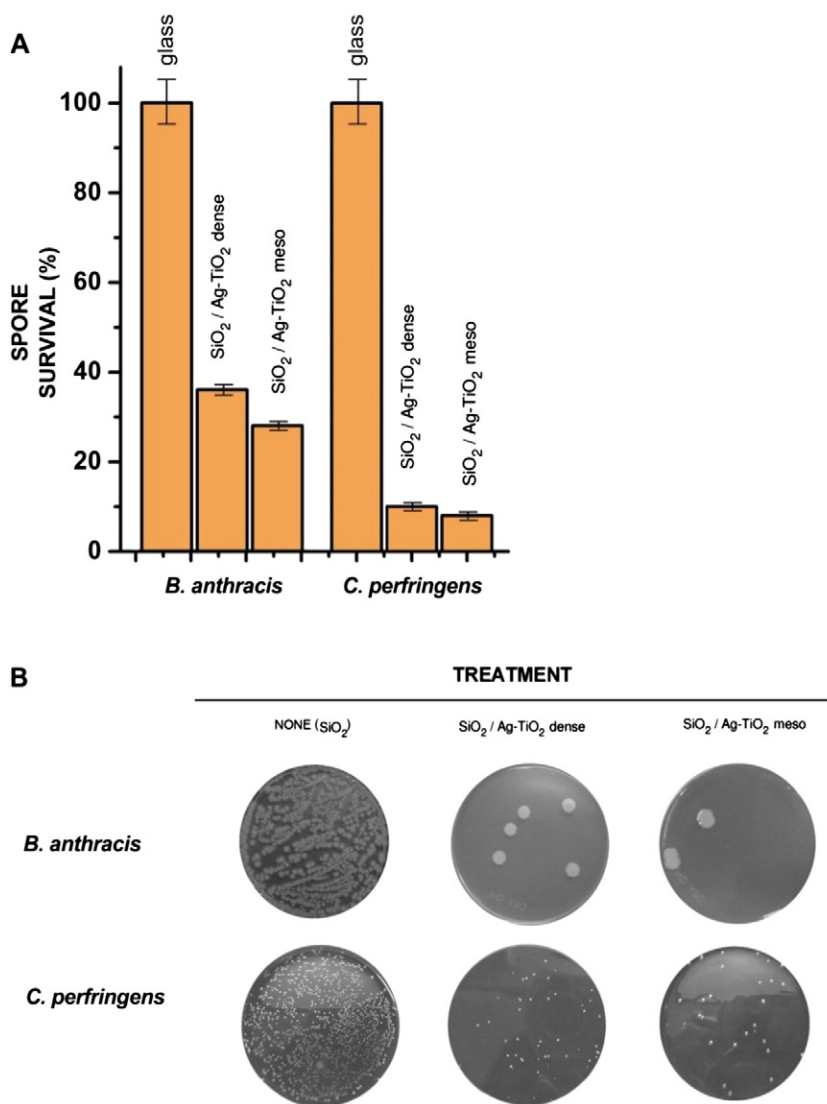


Fig. 6. Sporocidal activity of SiO₂/Ag-TiO₂ composites under UV irradiation. (A) Pure spore suspensions from *B. anthracis* and *C. perfringens* cultures were exposed to the biocidal activity of Ag nanoparticles combined with photocatalytic TiO₂. The survival spores were counted as CFU per milliliter, and the mean values of three independent experiments are shown. The error bars represent standard errors. The number of viable spores recovered from no-coated glass slices kept in a dark environment or after 3 h of UV irradiation did not differ significantly from one another and correspond to 100% survival. (B) Germination ability of bacterial spores after treatment with silver nanoparticles embedded in dense and mesoporous TiO₂. The images correspond to digital photographs of BHI agar plates containing viable CFU recovered from 1×10^6 dilution of *B. anthracis* and *C. perfringens* spores after the stated treatments and incubated O/N at 37 °C under aerobic or anaerobic conditions for *B. anthracis* and *C. perfringens*, respectively.

samples have the smallest silver nanoparticles and they are placed in the outer layer. The smallest silver nanoparticles are more reactive and the release of Ag⁺ ions is easier. On the other hand, diffusive processes favor the Ag⁺ release from the layer near the surface.

It is worth pointing out that the materials with the best bactericidal behavior are obtained when the Ag NPs are embedded in the outer TiO₂ layer, whereas the best photocatalyst behavior appears when the Ag NPs are in the inner SiO₂ layer. The difference between photocatalytic and bactericidal performances comes from the different mechanisms involved in each process. The increase of bactericidal activity is associated with an additive effect, where the bactericide activity of silver nanoparticles is added to the bactericide properties of TiO₂. Silver nanoparticles do not modify the TiO₂ bactericidal properties, but rather they contribute with their own bactericidal effect through silver ion release. Then, the increase of bactericidal activity is higher in samples in which silver nanoparticles are in the outer layer, more available to the environment. On the other hand, silver nanoparticles are not photocatalysts themselves. The best photocatalytic behavior is obtained from the

material that allows the maximum stability of silver nanoparticles. Silver nanoparticles are partially degraded (oxidized) during their incorporation to the TiO₂ layer. However, this does not occur when silver nanoparticles are added to the inner SiO₂ layer, thereby the highest photocatalytic activity is observed for Ag-SiO₂/TiO₂ samples since Ag NPs maintained their properties.

In this work, the synthesis technique to obtain multifunctional thin film coatings has been described. These films have improved photocatalytic and bactericidal properties and are able to functionalize different surfaces without modifying their esthetic properties. Thus, these coatings are feasible to be applied to multiple products of technological or daily use as equipment surfaces or window glasses, respectively.

4. Conclusions

Transparent SiO₂/TiO₂ (dense and mesoporous) coatings doped with silver nanoparticles were obtained by a sol-gel technique. Silver nanoparticles were alternatively embedded in SiO₂ or TiO₂ layers. Nanoparticles embedded in TiO₂ layers were partially degraded during the

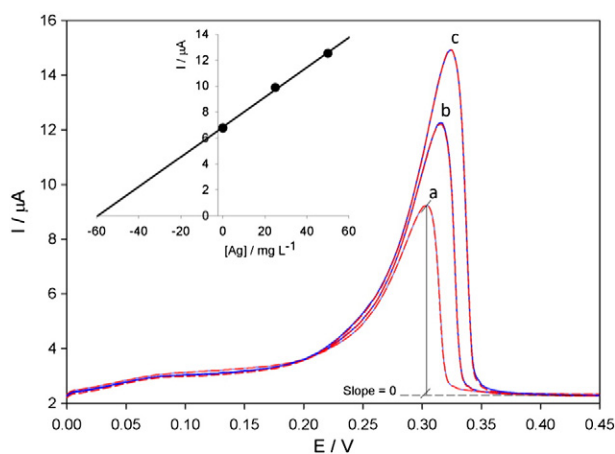


Fig. 7. Differential pulse anodic stripping voltammograms (DPASVs) registered in one representative aqueous sample, obtained after a 45 min exposure to $\text{SiO}_2/\text{Ag-TiO}_2$ dense surface. Each pair of curves display two independent scans corresponding to the standard addition method used to assess silver ions release. (a) DPASV of the sample, (b) DPASV after the addition of 0.025 mL of standard Ag^+ solution, and (c) DPASV after a further addition of 0.025 mL of standard Ag^+ . The inset shows the regression line obtained with the averaged signals (peak current) of each pair of scans as a function of $[\text{Ag}^+]$, minus X-intercept rendering silver concentration of the sample.

composite material synthesis. However, in TiO_2 mesoporous samples this effect was outweighed by the incorporation of a surfactant during the synthesis.

All samples show good photocatalytic and bactericidal activities and both properties are enhanced by doping with Ag nanoparticles. Further strengthening of the photocatalytic activity is observed when the nanoparticles are placed into the inner SiO_2 layer ($\text{Ag-SiO}_2/\text{TiO}_2$ dense and mesoporous samples). Mesoporous TiO_2 coatings are more active photocatalysts than the respective dense coatings because the increase of the specific surface area increases the contact between the photocatalytic material and the pollutant. From the experimental evidence, the pair separation of e-h contributes to the enhancement of photocatalytic activity, while the local field reinforcement is probably present. Also, a possible involvement of E_g shift and dispersion from nanoparticles is ruled out.

Further strengthening of the bactericidal properties is obtained when the Ag nanoparticles are placed into the TiO_2 layer, because they are more accessible to the environment. The increase of bactericidal activity is derived from the release of silver ions into the medium, even though the influence of other mechanisms is not ruled out.

Thus, the manipulation of the composite architecture allows tuning of the bactericidal and photocatalytic properties.

Supplementary data to this article can be found online at <http://dx.doi.org/10.1016/j.msec.2014.07.053>.

Acknowledgment

V.R. acknowledges the CONICET for the postdoctoral scholarship. The authors wish to thank Laura Peláez and Aritz Iglesias for their assistance with the experimental techniques and A. Olivieri for providing the spectrofluorophotometer. The authors also wish to thank the CONICET, the CSIC and the UNR for their financial support.

References

- [1] P. Robertson, J. Robertson, D. Bahnemann, J. Hazard. Mater. 211–212 (2012) 161–171.
- [2] D. Alrousan, P. Dunlop, T. McMurray, J. Byrne, Water Res. 43 (2009) 47–54.
- [3] D. Dourou, C.S. Beauchamp, Y. Yoon, I. Geornaras, K.E. Belk, G.C. Smith, G.J. Nychas, J.N. Sofos, Int. J. Food Microbiol. 149 (2011) 262–268.
- [4] P. Pichat, Appl. Catal. B Environ. 99 (2010) 428–434.
- [5] Q. Li, S. Mahendra, D. Lyon, L. Brunet, M. Liga, D. Li, P. Alvarez, Water Res. 42 (2008) 4591–4602.
- [6] S. Pal, Y. Tak, J. Song, Appl. Environ. Microbiol. 73 (2007) 1712–1720.
- [7] M. Rai, A. Yadav, A. Gade, Biotechnol. Adv. 27 (2009) 76–83.
- [8] G. Schmid (Ed.), Nanoparticles: From Theory to Application, Wiley-VCH, 2004.
- [9] C. Sanchez, L. Rozes, F. Ribot, C. Laberty-Robert, D. Grosso, C. Sasse, C. Boissiere, L. Nicole, C.R. Chim. 13 (2010) 3–39.
- [10] G. Soler-Illia, P. Angelomé, M. Fuertes, A. Calvo, A. Wolosiuk, A. Zelcer, M. Bellino, E. Martínez, J. Sol-Gel Sci. Technol. 57 (2011) 299–312.
- [11] B. Yu, K.M. Leung, Q. Guo, W.M. Lau, J. Yang, Nanotechnology 22 (2011) 115603.
- [12] M. Radzig, V. Nadtochenko, O. Koksharova, J. Kiwi, V. Lipasova, I. Khmel, Colloids Surf. B: Biointerfaces 102 (2013) 300–306.
- [13] K. Kulthong, S. Srisung, K. Boonpavanitchakul, W. Kangwansupamonkon, R. Maniratanachote, Part. Fibre Toxicol. 7 (2010) 8.
- [14] K. Zhang, M. Melo, L. Cheng, M. Weir, Y. Bai, H. Xu, Dent. Mater. 28 (2012) 842–852.
- [15] R. Kumar, H. Müntstedt, Biomaterials 26 (2005) 2081–2088.
- [16] O. Akhavan, E. Ghaderi, Surf. Coat. Technol. 204 (2010) 3676–3683.
- [17] P. Lalueza, M. Monzon, M. Arruebo, J. Santamaría, Mater. Res. Bull. 46 (2011) 2070–2076.
- [18] J. Davies, D. Davies, Microbiol. Mol. Biol. Rev. 74 (2010) 417–433.
- [19] E. Charani, J. Cooke, A. Holmes, J. Antimicrob. Chemother. 65 (2010) 2275–2277.
- [20] G. Di Bonaventura, R. Piccolomini, D. Paludi, V. D'Orto, A. Vergara, M. Conter, A. Ianieri, J. Appl. Microbiol. 104 (2012) 1552–1561.
- [21] R.F. Lamont, J. Sobel, S. Mazaki-Tovi, J.P. Kusanovic, E. Vaisbuch, S. Kim, N. Uldbjerg, R. Romero, J. Perinat. Med. 39 (2011) 227–236.
- [22] O. Disson, M. Lecuit, Virulence 3 (2012) 213–221.
- [23] K. Ireton, Cell. Microbiol. 9 (2007) 1365–1375.
- [24] Chi-Jung Wu, Po-Ren Hsueh, Wen-Chien Ko, J. Microbiol. Immunol. Infect. 44 (2011) 390–393.
- [25] C.L. Mayer, C.S. Leibowitz, S. Kurosawa, D.J. Stears-Kurosawa, Toxins 4 (2012) 1261–1287.
- [26] J.M. Rangel, P.H. Sparling, C. Crowe, P.M. Griffin, D.L. Swerdlow, Emerg. Infect. Dis. 11 (2005) 603–609.
- [27] M. Islam, M.P. Doyle, S.C. Phatak, P. Milner, X. Jiang, Food Microbiol. 22 (2005) 63–70.
- [28] M. Cooley, D. Carychao, L. Crawford-Miksza, M. Jay, C. Myers, C. Rose, C. Keys, J. Farrar, R. Mandrell, PLoS One 11 (2007) e1159.
- [29] M. Rai, S.D. Deshmukh, A.P. Ingle, A.K. Gade, J. Appl. Microbiol. 112 (2012) 841–852.
- [30] O. Akhavan, E. Ghaderi, Surf. Coat. Technol. 204 (2010) 3676–3683.
- [31] K. Chaloupka, Y. Malam, A.M. Seifalian, Trends Biotechnol. 28 (2010) 580–588.
- [32] H.H. Lara, N.V. Ayala-Núñez, L. Ixtepan Turrent, C. Rodríguez Padilla, World J. Microbiol. Biotechnol. 26 (2010) 615–621.
- [33] Wen-Ru Li, Xiao-Bao Xie, Quig-Shan Shi, Hai-Yan Zeng, You-Sheng OU-Yang, Yi-Ben Chen, Appl. Microbiol. Biotechnol. 85 (2010) 1115–1122.
- [34] M.J. Leggett, G. McDonnell, S.P. Denyer, P. Setlow, J.-Y. Maillard, J. Appl. Microbiol. 113 (2012) 485–498.
- [35] S.M. Cutting, Food Microbiol. 28 (2011) 214–220.
- [36] B. VidyalaXme, A. Rovetto, R. Grau, R. Agrawal, J. Food Sci. Technol. (2012), <http://dx.doi.org/10.1007/s13197-012-0834-5>.
- [37] K.-Y. Yoon, J.H. Byeon, J.-H. Park, Sci. Total Environ. 373 (2007) 572–575.
- [38] J.P. Ruparelia, A.K. Chatterjee, S.P. Duttgupta, S. Mukherji, Acta Biomater. 4 (2008) 707–716.
- [39] D.B. Hamal, J.A. Haggstrom, G.L. Marchin, M.A. Ikenberry, K. Hohn, K.J. Klabunde, Langmuir 26 (2010) 2805–2810.
- [40] A.M. Zand, S. Imani, M. Saadati, H. Honari, S. Rezaei-Zarchi, A. Javid, M. Zareh, M. Doroudian, Afr. J. Microbiol. Res. 6 (2012) 1417–1422.
- [41] S.-H. Lee, S. Pumprueg, B. Moudgil, W. Sigmund, Colloids Surf. B: Biointerfaces 40 (2004) 93–98.
- [42] J.A. Haggstrom, K.J. Klabunde, G.L. Marchin, Nanoscale 2 (2010) 399–405.
- [43] P.S.M. Dunlop, C.P. Sheeran, J.A. Byrne, M.A.S. McMahon, M.A. Boyle, K.G. McGuigan, J. Photochem. Photobiol. A Chem. 216 (2010) 303–310.
- [44] K. Page, R.G. Palgrave, I.P. Parkin, M. Wilson, S.L.P. Savin, A.V. Chadwick, J. Mater. Chem. 17 (2007) 95–104.
- [45] V. Philippe, M. Méndez, I.H. Huang, L. Orsaria, M.R. Sarker, R. Grau, Infect. Immun. 74 (2006) 3651–3656.
- [46] M. Méndez, I.H. Huang, K. Ohtani, R. Grau, T. Shimizu, M.R. Sarker, J. Bacteriol. 190 (2008) 48–60.
- [47] D.G. Bouzianas, Trends Microbiol. 17 (2009) 522–528.
- [48] A. Driks, Mol. Aspects Med. 30 (2009) 368–373.
- [49] C.K. Cote, S.L. Welkos, J. Bouze, Microbes Infect. 13 (2011) 1146–1155.
- [50] M. Méndez, A. Goñi, W. Ramirez, R. Grau, Microb. Pathog. 52 (2012) 85–91.
- [51] D.L. Stevens, M.J. Aldape, A.E. Bryant, Anaerobe 18 (2012) 254–259.
- [52] X. Li, J. Lenhart, Environ. Sci. Technol. 46 (2012) 5378–5386.
- [53] A. Frattini, N. Pellegrini, D. Nicastro, O. de Sanctis, Mater. Chem. Phys. 94 (2005) 148–152.
- [54] M.V. Roldán, L. Scaffardi, O. de Sanctis, N. Pellegrini, Mater. Chem. Phys. 112 (2008) 984–990.
- [55] M. Bordenave, A. Scarpettoni, M.V. Roldán, N. Pellegrini, A. Bragas, Mater. Chem. Phys. 139 (2013) 100–106.
- [56] N. Arconada, Y. Castro, A. Durán, Appl. Catal. A Gen. 385 (2010) 101–107.
- [57] S. Martínez, T. Serrano, I. Gómez, A. Hernández, Bol. Soc. Esp. Ceram. Vidrio 46 (2007) 97–101.
- [58] M.E. Pedrido, P. de Oña, W. Ramirez, C. Leñini, A. Goñi, R. Grau, Mol. Microbiol. 87 (2013) 348–367.
- [59] A. Arabolaza, A. Nakamura, M.E. Pedrido, L. Martelotto, L. Orsaria, R. Grau, Mol. Microbiol. 47 (2003) 1251–1263.
- [60] C. Balagué, L. Fernández, J. Pérez, R. Grau, J. Antimicrob. Chemother. 51 (2003) 401–404.
- [61] C. Liu, D. Yang, Y. Jiao, Y. Tian, Y. Wang, Z. Jiang, ACS Appl. Mater. Interfaces 5 (2013) 3824–3832.
- [62] M.V. Roldán, O. de Sanctis, N. Pellegrini, Opt. Mater. 33 (2011) 1921–1926.

- [63] A. Ismail, *Microporous Mesoporous Mater.* 149 (2012) 69–75.
- [64] X. Xue, W. Ji, Z. Mao, H. Mao, Y. Wang, W. Wang, W. Ruan, B. Zhao, J.R. Lombardi, J. *Phys. Chem. C* 116 (2012) 8792–8797.
- [65] M. Hari, S.A. Joseph, S. Mathew, P. Radhakrishnan, V.P. Nampoori, J. *Appl. Phys.* 112 (2012) 074307 (1–9).
- [66] N. Abazovic, M. Comor, M. Dramicanin, D. Jovanovic, S. Ahrenkiel, J. Nedeljkovic, J. *Phys. Chem. B* 110 (2006) 25366–25370.
- [67] J. Shi, J. Chen, Z. Feng, T. Chen, Y. Lian, X. Wang, C. Li, J. *Phys. Chem. C* 111 (2007) 693–699.
- [68] J. Zhou, Y. Zhang, X.S. Zhao, A.K. Ray, *Ind. Eng. Chem. Res.* 45 (2006) 3503–3511.
- [69] S. Linic, P. Christopher, D. Ingram, *Nat. Mater.* 10 (2011) 911–921.
- [70] K. Awazu, M. Fujimaki, C. Rockstuhl, J. Tominaga, H. Murakami, Y. Ohki, N. Yoshida, T. Watanabe, *J. Am. Chem. Soc.* 130 (2009) 1676–1680.
- [71] P. Christopher, D. Ingram, S. Linic, J. *Phys. Chem. C* 114 (2010) 9173.